

A New Proposal to Jefferson Lab PAC48

Measurement of the Two-Photon Exchange contribution to the electron-neutron elastic scattering cross section

S. Alsalmi (spokesperson)

King Saud University, Riyadh 11451, Saudi Arabia

E. Fuchey (spokesperson) and A.J.R. Puckett

University of Connecticut, Storrs, Connecticut 06269, USA

B. Wojtsekowski (spokesperson), S. Barcus*, A. Camsonne*, J-P. Chen*,

D. Gaskell*, O. Hansen, D. W. Higinbotham, M. Jones, C. Keppel*,

D. Mack*, D. Meekins, R. Michaels, B. Sawatzky, G. Smith, and S. Wood*

Thomas Jefferson National Accelerator Facility, Newport News, Virginia 23606, USA

T. Averett

The College of William and Mary, Williamsburg, Virginia 23185, USA

K. Aniol

California State University, Los Angeles, CA 90032, USA

V. Bellini*

Istituto Nazionale di Fisica Nucleare, I-95123 Catania, Italy

W. Boeglin and P. Markowitz

Florida International University, Miami, FL 33199, USA

G. Cates*, K. Gnanno*, C. Gu*, J. Liu*, N. Liyanage*, V. Nelyubin*, and C. Palatchi*

University of Virginia, Charlottesville, Virginia 232904, USA

E. Cisbani, F. Meddi*, and G. Urciuoli*

*Istituto Nazionale di Fisica Nucleare - Sezione di Roma,
P.le Aldo Moro, 2 - 00185 Roma, Italy*

J.C. Cornejo* and B. Quinn*

Carnegie Mellon University, Pittsburgh, Pennsylvania 15213, USA

B. Crowe* and B. Vlahovic*

North Carolina Central University, Durham, North Carolina 27707, USA

C. Gayoso

Mississippi State University, Mississippi State, MS 39762, USA

D. Hamilton and R. Montgomery

SUPA School of Physics and Astronomy,

University of Glasgow, Glasgow G12 8QQ, UK

F. Hauenstein

Old Dominion University, Norfolk, Virginia 23529, USA

A. T. Katramatou and G.G. Petratos

Kent State University, Kent, OH 44242, USA

D. Nguyen and A. Schmidt

Massachusetts Institute of Technology, Cambridge, MA 02139, USA

C. Petta* and C. Suttera*

Istituto Nazionale di Fisica Nucleare, Dipt. di Fisica dell Univ. di Catania, I-95123 Catania, Italy

P. Reimer*

Argonne National Laboratory, 9700 S Cass Ave, Lemont, Illinois 60439, USA

A. Sarty

Saint Mary's University, Halifax, Nova Scotia B3H 3C3, Canada

K. Slifer*

University of New Hampshire, Durham, NH 03824, USA

A. Shahinyan

AANL, 2 Alikhanian Brothers Street, 0036, Yerevan, Armenia

S. Širca*

Faculty of Mathematics and Physics, University of Ljubljana, 1000 Ljubljana, Slovenia

E. Voutier*

Institut de Physique Nucléaire, 15 Rue Georges Clemenceau, 91400 Orsay, France

(Dated: June 11, 2020)

Abstract

We propose to make a high precision measurement of the two-photon exchange contribution (TPE) in elastic electron-neutron scattering at a four-momentum transfer $Q^2 = 4.5$ $(\text{GeV}/c)^2$. While significant efforts to study the two-photon-exchange have focused around elastic electron-proton scattering, the impact of TPE on neutron form factors was never examined experimentally. The proposed experiment will provide the very first assessment of the two-photon exchange in electron-neutron scattering, which will be important for understanding the nucleon form factor physics.

The proposed experiment will be performed in Hall A using the BigBite (BB) spectrometer to detect the scattered electrons and the Super-BigBite (SBS) to detect the protons and neutrons. The experiment should run concurrently with the E12-09-019 G_M^n and E12-17-004 G_E^n -Recoil experiments, which are expected to run in 2021. The experimental setup of the proposed experiment will be identical to that of E12-09-019 experiment.

The “ratio” method will be used to extract the electric form factor of the neutron G_E^n by scattering unpolarized electrons from deuterium quasi-elastically at two beam energies 4.4 and 6.6 GeV and electron scattering angles 41.9 and 23.3 degrees respectively. In the proposed approach, systematic errors are greatly reduced compared to those in the traditional single electron arm configuration. Several experiments at Mainz and JLab have used the ratio method to measure the neutron magnetic form factor in the past years. The method can be extended to extract the neutron electric form factor even with less stringent requirements on the knowledge of the absolute neutron detection efficiency and experimental kinematics.

I. INTRODUCTION

In 1950's, a series of experiments performed by R. Hofstadter [1] revealed that the nucleons have a substructure (would be called later the quarks and gluons). The experiment confirmed M. Rosenbluth's theory [2] based on one-photon exchange approximation. In the Born approximation, where the interaction between the electron and the nucleon occurs *via* an exchange of a one virtual photon (OPE), the unpolarized $e - N$ elastic cross section can be expressed in terms of a nucleon magnetic, G_M , and electric, G_E , form factors. These form factors describe the deviation from a point-like scattering cross section:

$$\left(\frac{d\sigma}{d\Omega} \right)_{eN \rightarrow eN} = \frac{\sigma_{Mott}}{\epsilon(1 + \tau)} [\tau \cdot G_M^2(Q^2) + \epsilon \cdot G_E^2(Q^2)] = \sigma_T + \epsilon \cdot \sigma_L, \quad (1)$$

where E and E' are the incident and scattered electron energies, respectively, θ is the electron scattering angle, $\tau \equiv -q^2/4M^2$, with $-q^2 \equiv Q^2 = 4EE' \sin(\theta/2)$ being the negative four momentum transfer square, M is the nucleon mass, and $\epsilon = [1 + 2(1 + \tau) \tan^2(\theta/2)]^{-1}$ is the longitudinal polarization of the virtual photon, σ_L and σ_T are the cross sections for longitudinally and transversely polarized virtual photons, respectively.

The linear ϵ dependence of the cross section is due to σ_L term, see Eq. 1. The ratio σ_L/σ_T is a Rosenbluth slope related to G_E/G_M (in OPE), see Fig. 1. The data show that at Q^2 of 4-5 $(\text{GeV}/c)^2$ the Rosenbluth slope is three-four times larger than it suppose to be (in OPE) for the observed values of the G_E^p/G_M^p ratio.

The nucleon electromagnetic form factors can reveal a lot of information about the nucleon internal structure, as well as the quark distribution. The form factors depend only on one variable the negative square of the four-momentum transfer carried by the photon, Q^2 . In the limit of large Q^2 , pQCD provides well-motivated predictions for the Q^2 -dependance of the form factors and their ratio. However, it was never predicted at what Q^2 range the pQCD prediction (scaling) will be valid. Studies of GPDs show that pQCD validity will require a very large Q^2 of 100 $(\text{GeV}/c)^2$. It was discovered at JLab, using the double polarization methods, that the proton electric and magnetic form factors behave differently starting at

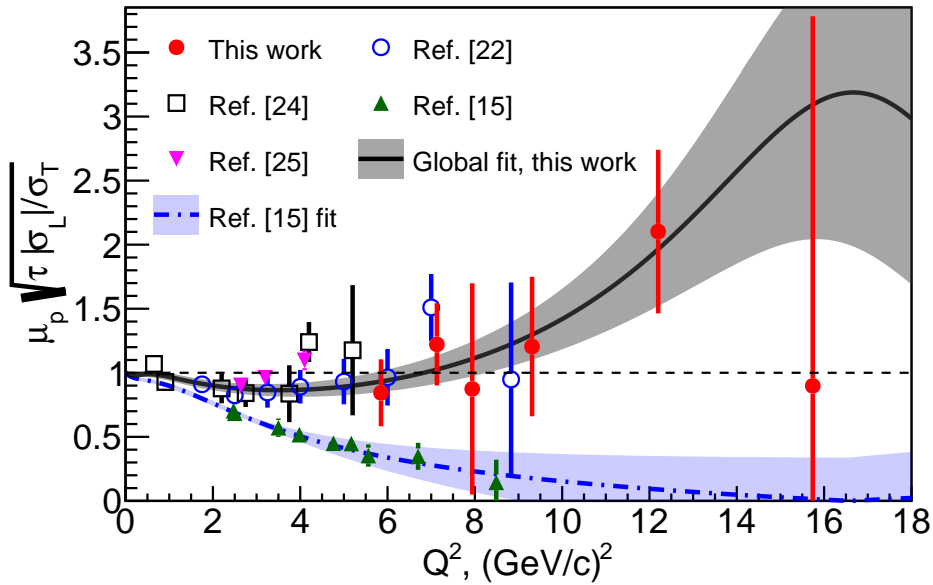


FIG. 1. The square root of Rosenbluth slope, corrected for kinematical factor $\sqrt{\tau}$ and μ_p , observed in elastic electron-proton scattering, adopted from Ref. [3].

²⁷ $Q^2 \approx 1 \text{ (GeV/c)}^2$.

²⁸ Experimentally, the nucleon form factors can be measured using one of two techniques:
²⁹ polarization transfer technique and Rosenbluth technique. The polarization method exam-
³⁰ ines the polarization transfer from longitudinally polarized electron to the recoiling nucleon
³¹ and determine the resulting azimuthal asymmetry distribution using a polarimeter. Alter-
³² natively, one can use the polarized electron beam and a polarized target. While in the
³³ Rosenbluth method, the electric and magnetic form factors can be separated by making
³⁴ two or more measurements with different ϵ values (*i.e.* different beam energies and angles),
³⁵ but with same Q^2 value. Rosenbluth technique requires an accurate measurement of the
³⁶ cross section and suffers from large systematic uncertainties arising from several factors. For
³⁷ instance, an accurate knowledge of the neutron detector efficiency is required.

³⁸ When comparing the values of G_E^p/G_M^p obtained from both techniques, a significant dis-
³⁹ crepancy was observed (see Fig. 1). Such discrepancy implies a potential problem in our
⁴⁰ understanding of the nucleon substructure. Many efforts were made in order to provide
⁴¹ legitimate explanation, and it is believed that the inconsistency is due to contribution of

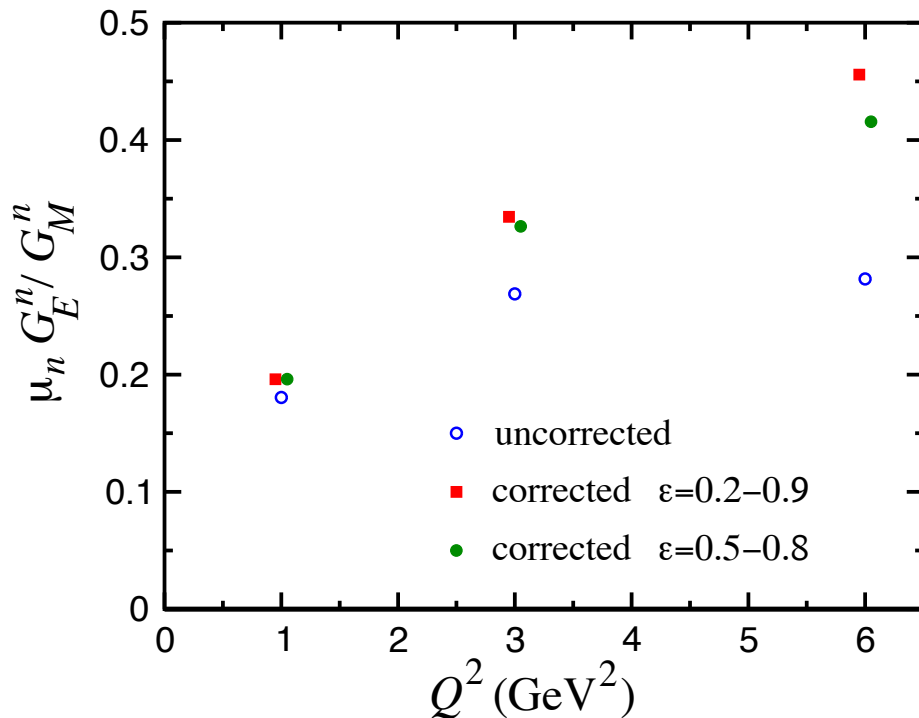


FIG. 2. Projected impact of TPE on G_E^n/G_M^n using LT separation, according to Ref. [4].

⁴² two-photon exchange in $e - N$ elastic scattering process, see Refs. [5, 6]. Predictions made
⁴³ for the neutron case are shown in Fig. 2 , adopted from [4]. The contribution of TPE could
⁴⁴ reach about 30% of Rosenbluth slope value at 5 (GeV/c) 2 .

⁴⁵ In the following we propose to make precision L/T separation of the elastic electron-
⁴⁶ neutron cross section and first experimental assessment of the two-photon exchange contri-
⁴⁷ bution on the neutron magnetic form factor measurements (see also Ref. [7]). The result of
⁴⁸ the nTPE experiment will likely add a new component to our understanding of the elastic
⁴⁹ electron-nucleon process.

50

II. PHYSICS MOTIVATION

51 The nucleon plays the same central role in hadronic physics that the hydrogen atom does
 52 in atomic physics and the deuteron in the physics of nuclei. The structure of the nucleon
 53 and its specific properties, such as charge, magnetic moment, size, mass; the elastic electron
 54 scattering form factors, resonances; and structure functions in DIS, are of fundamental sci-
 55 entific interest. The isospin is a fundamental property of the nucleon, so both the proton and
 56 neutron investigations are important to do. By using data on the proton and neutron form
 57 factors the flavour structure could be explored [8]. It is already provided the most direct
 58 evidence for a diquark correlation in the nucleon [9–11].

59 Hadron structure, as seen in elastic electron scattering, in one-photon approximation,
 60 defined by two functions of four momentum transfer square. They are: the helicity conserving
 61 Dirac form factor, F_1 , which describes the distribution of the electric charge, and the helicity
 62 non-conserving Pauli form factor, F_2 , describes the distribution of the magnetic moment.
 63 These two form factors are the ingredients of the hadronic current. These form factors
 64 contain information on the transverse charge distribution for an unpolarized and transversely
 65 polarized nucleon, respectively, in the infinite momentum frame [12, 13].

66 The Sachs form factors, G_E and G_M , the ratio of which will be extracted directly from
 67 the data, are related to F_1 and F_2 by

$$F_1 = \frac{G_E + \tau G_M}{1 + \tau} \text{ and } F_2 = \frac{G_M - G_E}{\kappa(1 + \tau)}, \quad (2)$$

68 where κ is the nucleon anomalous magnetic moment.

69 Already twenty four years ago, important developments in QCD phenomenology has
 70 been the exploration of the generalized parton distribution (GPD) formalism [14–16], which
 71 provides relations between inclusive and exclusive observables. The nucleon elastic form
 72 factors F_1 and F_2 are given by the first moments of the GPDs

$$F_1(t) = \sum_q \int_0^1 H^q(x, \xi, t, \mu) dx \text{ and } F_2(t) = \sum_q \int_0^1 E^q(x, \xi, t, \mu) dx, \quad (3)$$

73 where H^q and E^q are two of the generalized parton distributions, x is the standard Bjorken
 74 x , ξ is the “skewness” of the reaction, t is the four-momentum transferred by the electron,

⁷⁵ μ is a scale parameter necessary from the evolution over Q^2 , analogous to DIS parton distributions, and the sum is over all quarks and anti-quarks. These may be accessed through processes such as deeply virtual Compton scattering, where the interaction is factorized into a hard part with the virtual photon/photon interactions with an individual quark and a soft part of the residual system where the GPD information is contained.

⁸⁰ Fundamental nucleon feature, the spin, is related to GPDs, as shown by X. Ji [15]. The moments of GPDs can yield information, according to the Ji's Angular Momentum Sum Rule, on the contribution to the nucleon spin from quarks and gluons, including both the quark spin and orbital angular momentum.

⁸⁴ At present, experimental measurements of GPDs are still scarce. Until high Q^2 DVCS data becomes available, work has been done to attempt to parameterize these GPDs, which rely heavily on data from electromagnetic form factors and parton distributions from DIS as constraints [17]. Data at high Q^2 for G_E^n would contribute significantly in the development of these models.

⁸⁹ As we presented above the form factors are important components for GPDs development. However, the cross section of elastic $e-p$ scattering contains a significant contribution to σ_L , which at high Q^2 is much larger than theory calculations expected [18]. Such an alarming observation underlines that understanding of TPE effect is essential for hadron physics.

93

III. TECHNIQUE

94 The neutron form factors are challenging to be determine experimentally especially be-
 95 cause there is no free neutron target. However, since the deuterium is a loosely coupled
 96 system, it can be viewed as the sum of a proton target and a neutron target. In fact, quasi-
 97 elastic scattering from deuterium has been used to extract the neutron magnetic form factor,
 98 G_M^n , at modestly high Q^2 for decades [19, 20] in the single arm (e, e') experiments. How-
 99 ever, the proton cross section needs to be subtracted by applying a single-arm quasi-elastic
 100 electron-proton scattering. This “proton-subtraction” technique suffers from a number sys-
 101 tematic uncertainties e.g. contributions from inelastic and secondary scattering processes.

102 Many year ago, L. Durand [21] proposed the so-called “ratio-method” based on the mea-
 103 surement of both $D(e, e'n)$ and $D(e, e'p)$ reactions. In this method, many of the systematic
 104 errors are cancel out. Several experiments [22–24] have applied the ratio-method to determine
 105 the neutron magnetic form factor. We propose to use this method to measure Rosenbluth
 106 slope and extract (in OPE approximation) the neutron electric form factor, G_E^n .

107 Data will be collected for quasi-elastic electron scattering from deuteron in process
 108 $D(e, e'n)p$. A complementary $D(e, e'p)n$ data will be taken to calibrate the experiment ap-
 109 paratus. The current knowledge of the $e - p$ elastic scattering cross section (obtained in the
 110 single arm $H(e, e')p$ and $H(e, p)e'$ experiments) will be also used for precision determination
 111 the experiment kinematics.

112 Applying Rosenbluth technique to measure G_E^n requires accurate measurement of the cross
 113 section and suffers from large uncertainties. To overcome this issue, we propose to extract
 114 the value of G_E^n from the measured the ratio of quasi-elastic yields, $R_{n/p}$, in scattering from
 115 a deuteron target as follows:

$$R_{n/p} \equiv R_{observed} = \frac{N_{e, e'n}}{N_{e, e'p}} \quad (4)$$

116 $R_{observed}$ needs to be corrected to extract the ratio of e-n/e-p scattering from nucleons:

$$R_{corrected} = f_{corr} \times R_{observed} , \quad (5)$$

117 where the correction factor $f_{correction}$ takes into account the variation in the hadron efficiencies
 118 due to changes of $e - N$ Jacobian, the radiative corrections, and absorption in path from the
 119 target to the detector, and small re-scattering correction.

120 In one-photon approximation, $R_{corrected}$ can be presented as:

$$R_{corrected} = \frac{\sigma_{Mott}^n \cdot (1 + \tau_p)}{\sigma_{Mott}^p \cdot (1 + \tau_n)} \times \frac{\epsilon \sigma_L^n + \sigma_T^n}{\epsilon \sigma_L^p + \sigma_T^p} \quad (6)$$

It is important that the ratio $R_{Mott} = \frac{\sigma_{Mott}^n \cdot (1 + \tau_p)}{\sigma_{Mott}^p \cdot (1 + \tau_n)}$ could be determined with very high relative accuracy even with modest precision for the beam energy, electron scattering angle, and detector solid angle. Now, let us write the $R_{corrected}$ at two values of ϵ using $R_c^{n(p)} = \sigma_L^{n(p)} / \sigma_T^{n(p)}$ as:

$$R_{corrected,\epsilon_1} = R_{Mott,\epsilon_1} \times \frac{\epsilon_1 \sigma_L^n + \sigma_T^n}{\epsilon_1 \sigma_L^p + \sigma_T^p} \quad R_{corrected,\epsilon_2} = R_{Mott,\epsilon_2} \times \frac{\epsilon_2 \sigma_L^n + \sigma_T^n}{\epsilon_2 \sigma_L^p + \sigma_T^p}$$

In these two equations there are two unknown variables: σ_L^n and σ_T^n . The dominant contribution to the uncertainty of the slope of the cross section vs. ϵ , $S_c^n = \sigma_L^n / \sigma_T^n$, will come from the uncertainty of S_c^p . At $Q^2=4.5$ (GeV/c)², according to the global analysis of $e - p$ cross section [3], the value of S_c^p is close to $1/(\tau \mu_p^2) = 0.107$ with uncertainty of 0.01. The resulting equation for S_c^n is:

$$A = B \times \frac{1 + \epsilon_1 S_c^n}{1 + \epsilon_2 S_c^n} \approx B \times (1 + \Delta \epsilon \cdot S_c^n),$$

121 where the variable $A = R_{corrected,\epsilon_1} / R_{corrected,\epsilon_2}$ will be measured with relative precision of
 122 0.1%. Assuming, for this estimate, equal values of Q^2 for two kinematics, the τ and σ_T for
 123 two kinematics are canceled out, and the variable $B = R_{Mott,\epsilon_1} / R_{Mott,\epsilon_2} \times (1 + \epsilon_2 S_c^p) / (1 + \epsilon_1 S_c^p)$.
 124 For actual small range of ϵ and small value of the slope, the $B \approx (1 - \Delta \epsilon \cdot S_c^p)$. The value
 125 of B will be determined from global proton $e - p$ data to a precision of 0.25×0.01 .

126 At $Q^2=4.5$ (GeV/c)² the ratio $\mu_n G_E^n / G_M^n$ is of 0.55 ± 0.05 , see the review [25]. In a
 127 simplest model, the slope S_c^n is a sum of the slope due to G_E^n / G_M^n and the TPE contribution.
 128 If we use for TPE the prediction [4], shown in Fig. 2, the TPE leads to increase of S_c^n by a
 129 factor of 2, so the result of this experiment for TPE will be $0.069 \pm 0.012 \pm 0.01$, where the
 130 first uncertainty is due to accuracy of G_E^n / G_M^n and the second one due to projected precision
 131 of this experiment. It would be a 4-4.5 sigma observation of the neutron TPE.

132

IV. EXPERIMENTAL SETUP

133 As illustrated in Fig. 3, this experiment will study electron scattering from a 15 cm
 134 long liquid Deuterium target held in a vacuum. The scattered electron will be detected
 135 in the BigBite spectrometer with an upgraded electron detector stack. The neutron arm is
 136 arranged with a dipole magnet 48D48 (SBS) and a segmented hadron calorimeter HCAL. The
 137 whole detector package was designed and is now under assembling for the GMn, E12-09-019,
 138 experiment.

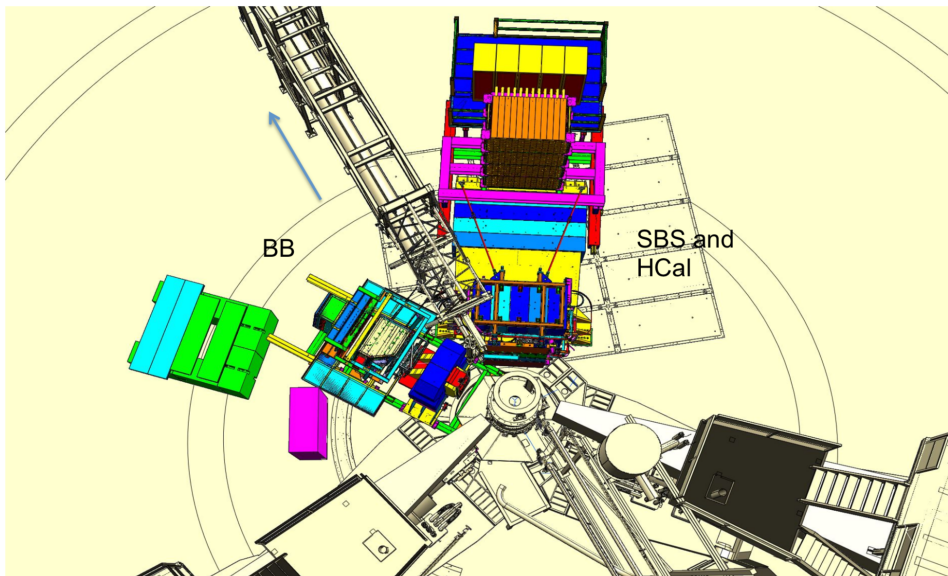


FIG. 3. Layout of the experimental setup in nTPE.

139

1. Parameters of the SBS

140 The 48D48 magnet from Brookhaven was acquired as part of the Super Bigbite project
 141 and will be available for this experiment. It consists of a large dipole magnet which provides
 142 a field integral of about $1.7 \text{ T} \cdot \text{m}$, allowing for quasielastic protons to be sufficiently deflected
 143 to allow clear differentiation from neutrons. The active field volume has an opening of $46 \times$
 144 $25 \text{ vertical} \times \text{horizontal}$), matching the aspect ratio of the neutron arm, and a depth of 48
 145 cm.

¹⁴⁶ The placement of this magnet will be 1.6 m away from the target, which would normally
¹⁴⁷ interfere with the beamline. To accommodate this, modifications were made to the iron yoke
¹⁴⁸ such that the beamline will pass through the magnet yoke area.

¹⁴⁹ The field configuration will be such that positively charged particles will be deflected
¹⁵⁰ upwards away from the hall floor. For a field integral of 1.7 Tesla-m, protons of momentum
¹⁵¹ 2.5 GeV/c will be deflected 250 mrad, which translates to a displacement of xxm. Including
¹⁵² expected detector resolution, the $p_{miss,\perp}$ distribution will be similar to what was seen in
¹⁵³ E02-013, so cuts of < 100 MeV/c will be appropriate. Monte Carlo simulations show a
¹⁵⁴ contamination of charged quasielastics to be negligible.

¹⁵⁵ The presence of the magnet also works to sweep low energy charged particles from the
¹⁵⁶ target away from the neutron arm. Particles of momentum less than 1.3 GeV/c will be
¹⁵⁷ entirely swept outside of the neutron arm acceptance. This greatly reduces the amount of
¹⁵⁸ charged low energy background.

159

A. The BigBite Spectrometer

160 Scattered electrons will be detected in the BigBite spectrometer. The spectrometer con-
 161 sists of a single dipole magnet (with magnetic field approximately 1.2 T) and a detection
 162 system, see Fig. 4.

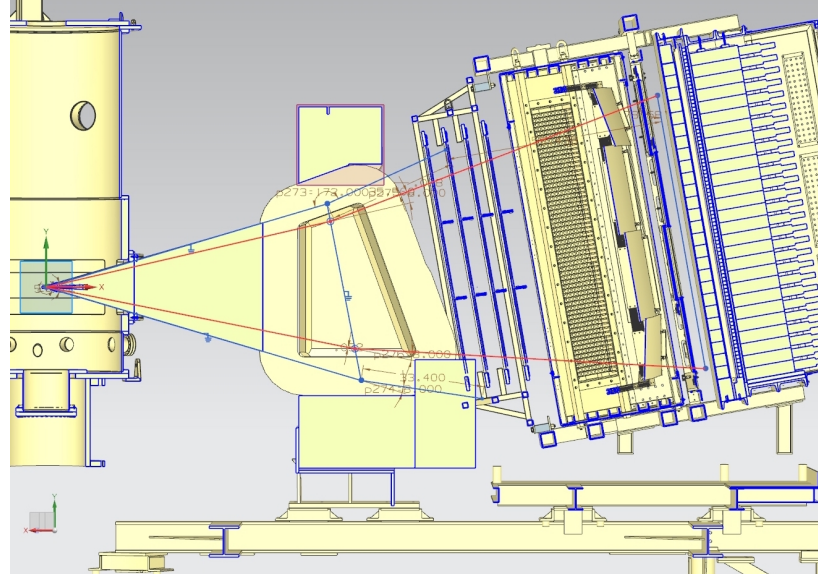


FIG. 4. The BigBite spectrometer with the upgraded detector stack.

163

1. GEM Chambers

164 To perform the tracking of charged particles under the high rates anticipated for this
 165 experiment, the drift chambers were replaced with gas electron multiplier (GEM) detectors.
 166 These detectors have proven to be capable of operating under luminosities of 25 kHz/mm^2
 167 for the COMPASS experiment at CERN and the spatial resolution of each of these chambers
 168 is anticipated to be about $70 \mu\text{m}$. There will be two sets of GEMs placed on each side of the
 169 GRINCH Cherenkov detector.

170 The set of GEMs in front of the GRINCH is composed of four layers of GEMs. Two of
 171 these layers have been built by will the SBS collaborators from INFN. They are composed

¹⁷² three modules each, measuring $40 \times 50 \text{ cm}^2$, such that each layer covers $40 \times 150 \text{ cm}^2$ (the
¹⁷³ long dimension being vertical, along the dispersive direction). The readout of these modules
¹⁷⁴ are oriented in the x/y direction *i.e.* parallel and perpendicular to the dispersive direction
¹⁷⁵ (horizontal and vertical). The two other layers are being built by the SBS collaborators from
¹⁷⁶ UVA. They are composed of a single module measuring $40 \times 150 \text{ cm}^2$, the long dimension
¹⁷⁷ again being vertical and along the dispersive direction. The readout of these modules are
¹⁷⁸ oriented in the u/v direction *i.e.* ± 30 degrees with respect to the horizontal direction.

¹⁷⁹ The set of GEMs behind the GRINCH has been built by the SBS collaborators from
¹⁸⁰ UVA. It is composed of a single layer composed of four modules measuring $50 \times 60 \text{ cm}^2$,
¹⁸¹ such that the layer covers $60 \times 200 \text{ cm}^2$ (the long dimension again being along the dispersive
¹⁸² direction). The readout of these modules are all oriented in the x/y direction.

¹⁸³ The level background in the GEMs have been evaluated, thanks to G4SBS ([\[?\]](#) abd
¹⁸⁴ Sec. [V](#)) for the G_M^n experimental readiness review. For the G_M^n highest Q^2 point (which is the
¹⁸⁵ most constraining, since it combines mandatory maximum luminosity and smaller BigBite
¹⁸⁶ angles, the background level in the front GEMs are of the order of 120 kHz/cm^2 for the front
¹⁸⁷ GEM layers, and below 50 kHz/cm^2 for the back GEM. To perform the GEM tracking within
¹⁸⁸ such a background environment, we use the cluster reconstructed in the BigBite shower as
¹⁸⁹ a track seed to clean the large combinatorics that would otherwise be created by the large
¹⁹⁰ number of hits. After this, the main challenge is the separation by the clustering algorithm
¹⁹¹ of the signal and background hits to minimize track smearing. At this level of background, a
¹⁹² TreeSearch tracking algorithm combined with a fairly simple cluster separation algorithm has
¹⁹³ already proven to achieve 70% efficiency at nominal luminosity. A better cluster separation
¹⁹⁴ algorithm is currently being developed and should allow to significantly improve this figure.

¹⁹⁵

2. Shower/Preshower

¹⁹⁶ The electromagnetic calorimeter configuration consists of two planes of lead glass blocks
¹⁹⁷ which we call the preshower and shower. The preshower, located about 80 cm behind
¹⁹⁸ the first GEM chamber, consists of a 2×26 plane of $37 \text{ cm} \times 9 \text{ cm}$ blocks. The shower, about
¹⁹⁹ 1 m behind the first GEM chamber, consists of an 7×27 array of $8.5 \text{ cm} \times 8.5 \text{ cm}$ blocks.

200 Sums over these blocks form the physics event trigger for the experiment.

201 The preshower signal can be used to provide an additional method of pion rejection.
202 By selecting low preshower signals, a pion rejection factor of 1:50 can be achieved through
203 optimization. Despite higher particle rates, pion rejection performance is anticipated to
204 be similar to that achieved for Transversity, E06-010. By measuring the pedestal widths
205 and resolution for E06-010 and scaling to this proposal's conditions, overall relative energy
206 resolution for the detector is expected to become worse by a factor of 1.6, to about $\sigma_{\delta E/E} =$
207 25%.

208 *3. Timing hodoscope*

209 The BigBite timing hodoscope has been built the the SBS collaborators from Glasgow,
210 to replace the BigBite scintillator plane. It will be composed of 90 bars stacked in a plane,
211 each with dimensions 1 in. \times 1 in. \times 60 cm. The paddle stack will be oriented such as
212 the long dimension of the bars is horizontal *i.e.* perpendicular to the dispersive direction.
213 Each of these elements are readout by a PMT on each side, mostly to provide measurement
214 redundancy.

215 This plane will primarily be used to provide a signal for nucleon time of flight reconstruc-
216 tion. A time resolution of 200 ps is anticipated. This fine segmentation is meant to lower the
217 rates in the detector. Background studies made for the G_M^n experimental readiness review [?]
218] demonstrated that the rates experienced by each element was \leq 500 kHz at a luminosity
219 of 2.8×10^{38} cm $^{-2}$ s $^{-2}$. The PMTs pulses are processed by NINO front-end cards which,
220 when the PMT pulse crosses the NINO threshold, will produce a digital signal to be readout
221 by CAEN 1190 TDCs which record a leading time and a trailing time.

222 *4. GRINCH cherenkov detector*

223 The main purpose of the Ring Imaging Cherenkov is to provide additional particle iden-
224 tification for offline pion rejection. The GRINCH consists of a tank with a maximum depth
225 of 88.9 cm, with 4 cylindrical mirrors focussing the cherenkov light directly onto a 510 PMT

²²⁶ array (60 lines of PMTs, with lines of 9 PMTs alternating with lines of 8 PMTs) placed away
²²⁷ from the beam. The radiation gas will be C_4F_8 , which is by far the best compromise between
²²⁸ light yield for electrons and operating cost. With $n - 1 = 1.35 \times 10^{-3}$, the π threshold is only
²²⁹ about 2.7 GeV, so the additional pion rejection will be most effective below this threshold.

²³⁰ As for the timing hodoscope The PMTs pulses are processed by NINO front-end cards
²³¹ which, when the PMT pulse crosses the NINO threshold, will produce a digital signal to
²³² be readout by VETROC TDCs, which for each PMT hit will record a leading time and a
²³³ trailing time. The analog signal will not be recorded however, which means that for each
²³⁴ PMT hit, the information of the number of not directly available (although it can in theory
²³⁵ be deduced from the time over threshold).

²³⁶ All of this implies that the electron selection relies on the number of GRINCH PMT
²³⁷ firing, instead of relying on the signal amplitude.

238

B. Hadron Calorimeter (HCal)

239 The Hadron Calorimeter (HCal) has been designed specifically to measure the recoil
 240 nucleon for the SBS experiments. Specifically for this experiment (and for G_M^n), HCal
 241 combined with the SBS (48D48) magnet provides identification of the recoil nucleon, as
 242 well as additional kinematic constraint and possibly timing information on the measured
 243 interaction. Nucleon identification is illustrated on Fig. 5. This figure shows the compared
 244 proton and neutron position distribution in HCal at the same electron kinematics. The
 245 proton distribution is being shifted upwards by about 1 m compared to the neutron.

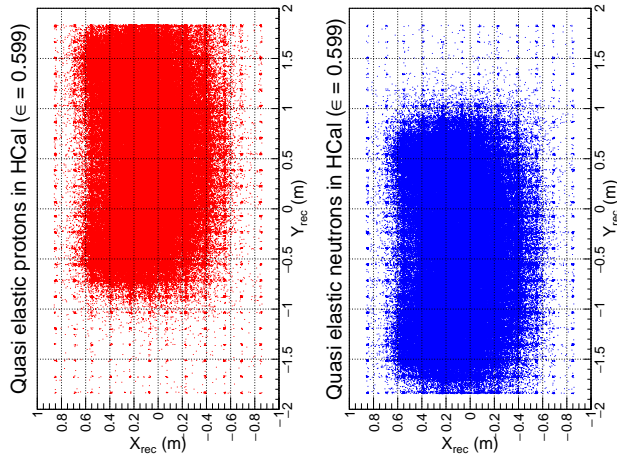


FIG. 5. Reconstructed HCal cluster from quasi-elastic events generated by G4SBS. The left distribution in red is for the proton, the right distribution in blue is for the neutron.

246

247

248 The HCal is composed of 288 modules arranged in an array of 12×24 (Fig. ??) In front
 250 of the full assembly is located a $3/4$ in steel plate which purpose is double:

- 251
 - initiate the hadronic shower to optimize the calorimeter response;
 - shield the modules from a fraction of the low energy secondaries;

253 Each of these modules measures $6 \times 6 \text{ in}^2$ section, for 3 ft length. They are composed of
 254 alternating tiles of scintillators and iron around a central light guide which collects the light

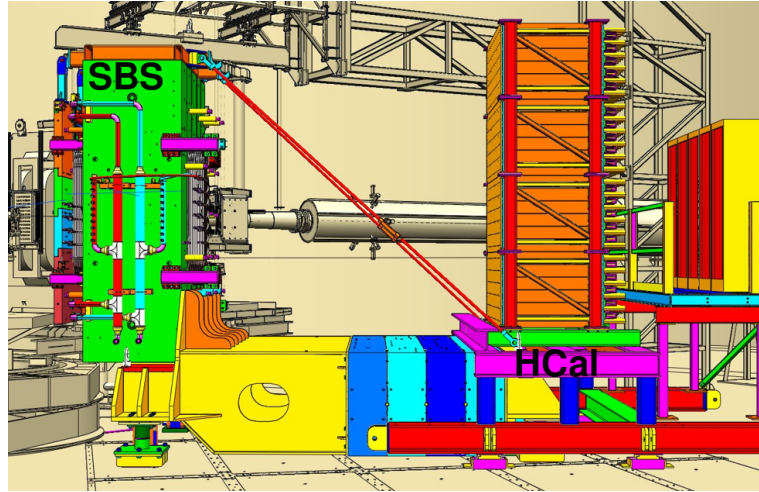


FIG. 6. CAD representation of HCal (right) with the SBS magnet (left)

generated in the scintillators by the hadronic shower, and guides it to the PMT at the end of the block. Cosmics tests have determined that the average light yield for the HCal modules is around 5 photoelectrons per MeV deposited in the scintillator tiles.

The PMTs are readout with FAD250 which sample the PMT signal every 40 ns and allow to reconstruct the PMT pulse shape, hence its timing. They are also readout by TDCs which provide additional timing information. Thanks to this, the timing resolution can be better than 1 ns, which cosmics tests (in progress) seem to confirm.

The energy resolution is intrinsically broad (see Fig. 9 in Section V), due mostly to the small fraction of energy from the hadronic shower actually measured by the scintillator tiles (≤ 0.1 - refer yet again to Fig. 9).

265 **V. SIMULATIONS, ESTIMATIONS OF COUNTING RATES AND**
 266 **ACCIDENTALS**

267 The estimations of counting rates accidentals have been performed using G4SBS, the
 268 GEANT4-based simulation package developed for the SBS experiment [?]. This package
 269 includes a wide range of event generators, which allows to evaluate the rates for both events
 270 of interest (signal) and background. The representation of the experiment apparatus in
 271 G4SBS is shown in the high ϵ configuration on Fig. 7.

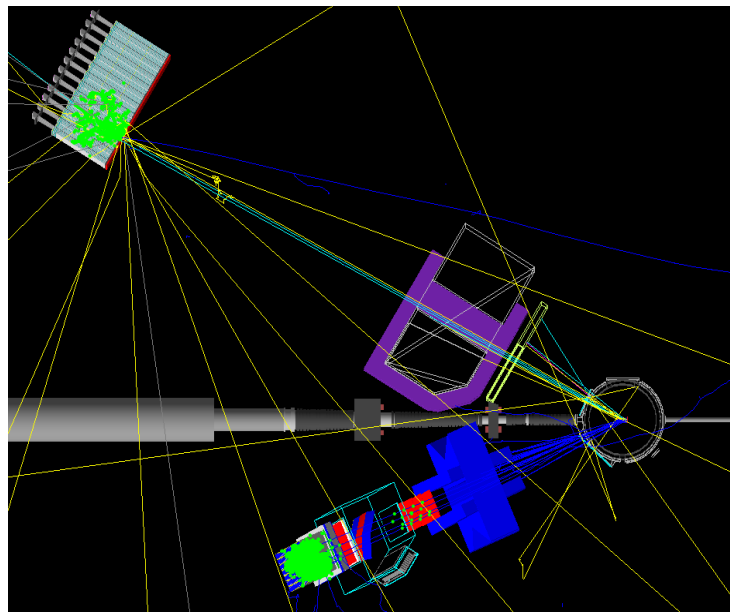


FIG. 7. Top view of the experimental apparatus model in G4SBS, shown in the high ϵ configuration. The beam direction is indicated, as well as the main elements (HCal, SBS magnet, BigBite spectrometer)

272
 273

274 **A. Background and trigger rates**

275 The main processes expected to contribute the trigger rates for the BigBite spectrometer
 276 are:

277 • the inelastic electron nucleon scattering process;

278 • photons from inclusive π^0 production;

279 • and to a lesser extent, charged pions.

280 One the other hand, we expect all sorts of hadronic backgrounds to contribute to the rates in
 281 HCal, the dominant ones being pions. Both the inelastic scattering and the inclusive neutral
 282 and charged pion production are implemented in G4SBS, the latter relying on the Wiser
 283 parametrization [?]. We may also considered the minimum-bias “beam-on-target” gener-
 284 ator for the HCal background, especially at lower angle (all electromagnetic and hadronic
 285 processes being built-in in G4SBS).

286 The thresholds to apply to each arm are determined as a function of the elastic peak. For
 287 the electron arm, the threshold has been set at $\mu_E - 2.5\sigma_E$, μ_E and σ_E being respectively
 288 the position and width of the fitted elastic peak. Fig. 8 presents the distributions of rate of
 289 energy deposit for the different processes involved in the BigBite trigger rates.

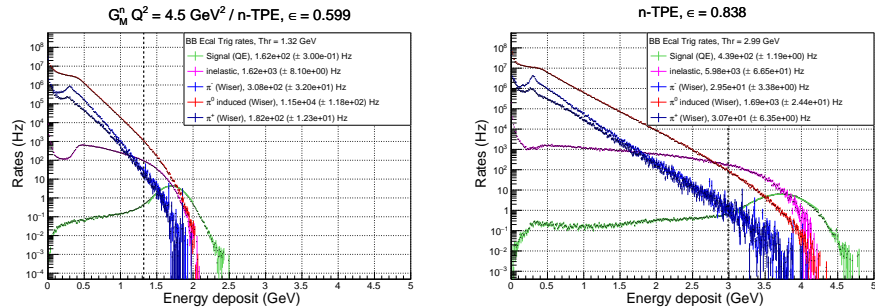


FIG. 8. Rates of the different process contributing to the BigBite electron arm trigger, for the low ϵ (left) and the high ϵ (right). Quasi-elastic is in green, inelastic in magenta, π^0 in red, π^- in blue, and π^+ in dark blue. Note the resolution for the elastic peak in the BigBite shower is ~ 0.3 GeV.

290

291

292 Since HCal is a sampling calorimeter (meaning that only a fraction of the shower energy
 293 is measured), it's resolution is significantly wider (~ 0.7 GeV). Due to this, the threshold
 294 is at 90% efficiency (which corresponds to ~ 0.1 GeV for both kinematics. Fig. 9 presents

295 the distributions of rate of energy deposit for the different processes involved in the BigBite
 296 trigger rates.

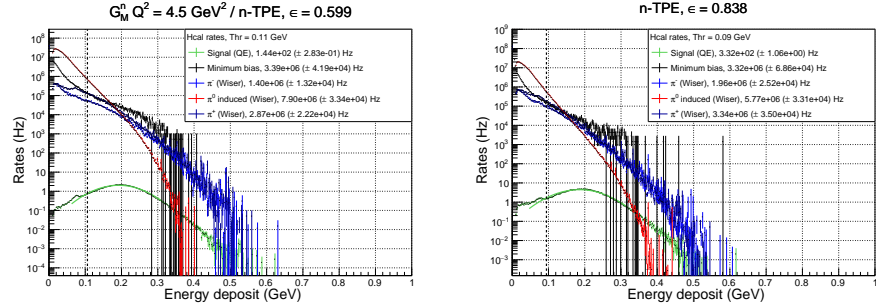


FIG. 9. Rates of the different process contributing to the HCal trigger, for the low ϵ (left) and the high ϵ (right). Quasi-elastic is in green, minimum bias in black, π^0 in red, π^- in blue, and π^+ in dark blue. Note the peak itself is around 0.2 GeV for 3.2 GeV nucleons.

297

298

299 The thresholds and trigger rates for each arm, as well as the coincidence rate (assuming
 300 30ns coincidence window), are summarized in Table. I.

301

302 Note that for HCal, the “total rates” is either the sum of inclusive charged and neutral pions
 303 evaluated with the Wiser cross sections *or* the “minimum bias” beam on target. We have
 304 good reasons to think that the Wiser code results actually overestimate the HCal rates, but
 305 for the sake of thoroughness, we have checked the coincidence rates assuming the sum of the
 306 inclusive pions (evaluated with the Wiser cross sections) as the HCal rates.

307 In the worst case scenario, the coincidence rates could be as high as 5kHz, which might be
 308 at the limit of manageability for the DAQ. However, a slight increase on the HCal threshold
 309 (which would drop the efficiency from ∼90% to ∼85%) would decrease the total HCal rates by
 310 ∼35% to 40% in this worst case scenario, which would make the situation more manageable
 311 (3.3 kHz).

Point (ϵ)	1 (0.599)		2 (0.838)	
	BigBite rates (Hz)	HCal rates (Hz)	BigBite rates (Hz)	HCal rates (Hz)
threshold (GeV)	1.32	0.106	2.99	0.090
Quasi-elastic	1.62×10^2	1.44×10^2	4.39×10^2	3.48×10^2
Inelastic	1.62×10^3	-	5.98×10^3	-
π^- (Wiser)	3.08×10^2	1.40×10^6	2.95×10^2	1.96×10^6
π^0 (Wiser)	1.15×10^4	7.90×10^6	1.69×10^3	5.77×10^6
π^+ (Wiser)	1.82×10^2	2.87×10^6	3.07×10^2	3.34×10^6
Minimum bias	-	3.39×10^6	-	3.32×10^6 (*)
<i>Total</i>	1.37×10^4	1.22×10^7	8.17×10^3	1.11×10^7
(min. bias - HCal only)		/ 3.39×10^6		/ 3.32×10^6
Coincidence rate	5.01×10^3		2.72×10^3	
(with min. bias HCal)	1.39×10^3		8.14×10^2	

TABLE I. Trigger rates for BigBite and HCal, with the different process contributions separated, and the sum. For HCal, the total rates is either the sum of the (Wiser) inclusive pions or the minimum bias. The coincidence rates assume a 30 ns coincidence window.

312 B. Accidentals: contamination from inelastic

313 The main source of contamination for the quasi-elastic comes from the inelastic electron-
 314 nucleon scattering. Most of this contamination can be cleaned out thanks to a selection on
 315 the center of mass energy

$$W^2 = M_N^2 + 2M_N^2(E - E') - Q^2, \quad (7)$$

316 and the missing transverse momentum of the nucleon

$$p_{\perp miss} = \sqrt{(q_x - p'_x)^2 + (q_y - p'_y)^2}, \quad (8)$$

317 where M_N is the mass of the nucleon, E and E' the initial and final energy of the electron,
 318 and $q_{x,y}$, $p'_{x,y}$ are the projections on x , y of the vectors of the virtual photon and final nucleon.

³¹⁹ The distributions of these quantities (weighted with cross section and including detector res-
³²⁰ olutions) are displayed for quasi-elastic and inelastic scattering, and for proton and nucleon,
³²¹ on Fig. 10 for the low ϵ kinematic, and on Fig. 11 for the high ϵ kinematic. Provided that

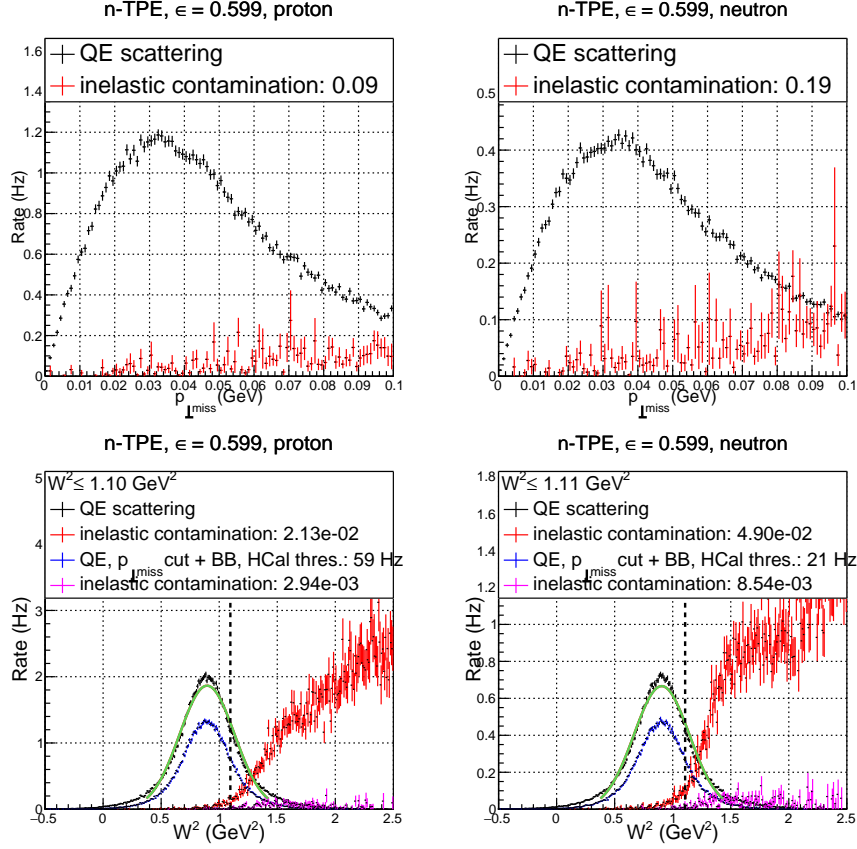


FIG. 10. Compared quasi-elastic and inelastic distributions (including detectors resolutions) for $p_{\perp miss}$ (top) and W^2 (bottom), for the low ϵ kinematic. Comparison for protons is on the left, and comparison for neutrons is on the right. On the bottom panel, black and red are before the $p_{\perp miss} \leq 0.1$ GeV selection, while blue and magenta are after $p_{\perp miss} \leq 0.1$ GeV selection and application of BigBite shower and HCal thresholds.

³²²

³²³

³²⁵ we are not limited by statistics and the sample purity is capital for our experiment, we set
³²⁶ the selection criteria on W^2 and $p_{\perp miss}$ to maximize inelastic contamination (ideally below
³²⁷ 1 %). Setting $p_{\perp miss} \leq 0.1$ GeV and $W^2 \leq 1.1$ GeV 2 , the inelastic contamination of the

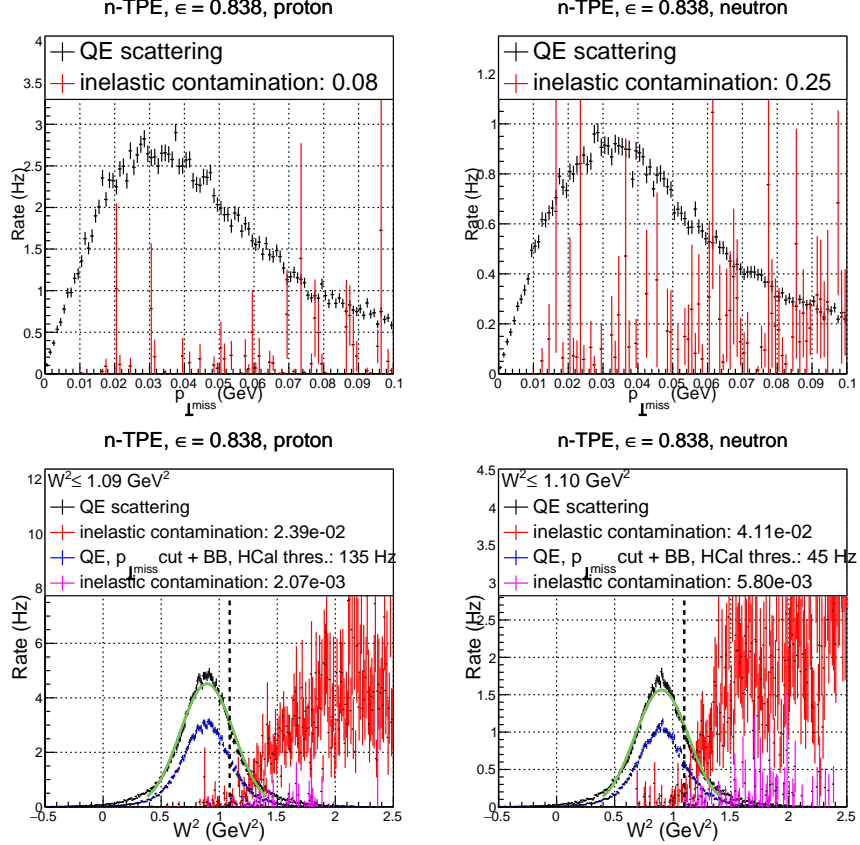


FIG. 11. Compared quasi-elastic and inelastic distributions (including detectors resolutions) for $p_{\perp\text{miss}}$ (top) and W^2 (bottom), for the high ϵ kinematic. Comparison for protons is on the left, and comparison for neutrons is on the right. On the bottom panel, black and red are before the $p_{\perp\text{miss}} \leq 0.1$ GeV selection, while blue and magenta are after $p_{\perp\text{miss}} \leq 0.1$ GeV selection and application of BigBite shower and HCal thresholds.

328 elastic sample ranges from 0.2 % to 0.9 %, while retaining ≥ 60 %.

329

C. Quasi-elastic counting rates

330 The signals for this experiment have been generated using the G4SBS elastic/quasi-elastic
 331 generator. We generated 1M events sample for each kinematics, on a solid angle that was
 332 larger than the detector acceptance. To evaluate the detector solid angle, we define simple

³³³ criteria that each event has to pass, defined as the following;

³³⁴ • require a primary track, going through all 5 GEM layers (electron arm);

³³⁵ • require non-zero energy deposit in both the preshower and shower (electron arm);

³³⁶ • require non-zero energy deposit in HCal (hadron arm).

³³⁷ The detector solid angle, for both proton and neutron, are defined in Table. II

Point (ϵ)	$\Delta\Omega_e$ (msr)	$\Delta\Omega_e \otimes \Delta\Omega_n$ (msr)	$\Delta\Omega_e \otimes \Delta\Omega_p$ (msr)
1 (0.599)	52.4	46.7	47.2
2 (0.838)	32.7	20.8	22.2

TABLE II. Kinematics electron solid angle, and convoluted electron/hadron solid angle

³³⁸

³³⁹ Then, we evaluate the detection efficiency. For the electron, we require the energy reconstructed in the BigBite calorimeter to be above a threshold defined as $thr = \mu_E - 2.5 * \sigma_E$,
³⁴⁰ as well as a minimum number of GRINCH PMTs fired due to the primary electron; For
³⁴¹ HCal, we require the threshold to be such as we obtain 90% efficiency. These values are
³⁴² summarized in Table. III.

Point (ϵ)	BB thr. (GeV)	HCal thr. (GeV)	$\eta_{det\ e}$	$\eta_{det\ n}$	$\eta_{det\ p}$	$\eta_{sel\ n}$	$\eta_{sel\ p}$
1 (0.599)	1.32	0.11	0.902	0.904	0.892	0.589	0.605
2 (0.838)	2.99	0.09	0.808	0.889	0.882	0.617	0.647

TABLE III. Kinematics electron thresholds, particle detection efficiencies (η_{det}), and efficiency of quasi-elastic selection η_{sel} separated for the proton and the neutron.

³⁴⁴

³⁴⁵ The counting rates are evaluated using the events that have passed the selection described
³⁴⁶ above, and weighting those events with the cross section calculated by G4SBS, multiplied
³⁴⁷ by the generation solid angle, using the formula:

$$N_{est} = \mathcal{L}\Delta t \times \sum_{i \in \text{accepted evts}} \frac{d\sigma}{d\Omega} * \Delta\Omega_{Gen}/N_{Gen} \quad (9)$$

³⁴⁸ Events are “accepted” if they meet the following criteria:

- ³⁴⁹ • the electron is in the BigBite acceptance;
- ³⁵⁰ • the electron passes the BigBite threshold defined in Table III and gives signal in the
³⁵¹ GRINCH;
- ³⁵² • the nucleon is in the HCal acceptance and passes the HCal threshold defined in Ta-
³⁵³ ble III;
- ³⁵⁴ • the event passes the quasi-elastic selection defined in the previous section *i.e.* $W^2 \leq 1.1 \text{ GeV}^2$
³⁵⁵ and $p_{\perp miss} \leq 0.10 \text{ GeV}$.

³⁵⁶ The counting rates, as well as the reduced cross section F^2 and its error $\Delta F^2 = F^2/\sqrt{N_{QE}}$
³⁵⁷ are compiled for both kinematics in Table. IV, assuming a running time $\Delta t = 12$ hours of
³⁵⁸ running at a beam intensity of $I_{exp} = 30 \mu\text{A}$ on a liquid deuterium target with length
³⁵⁹ $l_{tgt} = 15 \text{ cm}$ and density $d_{tgt} = 0.169 \text{ g.cm}^{-3}$.

Point (ϵ)	QE $e-n$ counts	QE $e-p$ counts	F_n^2 ($\times 10^{-3}$)	ΔF_n^2 ($\times 10^{-6}$)	F_p^2 ($\times 10^{-3}$)	ΔF_p^2 ($\times 10^{-6}$)
1 (0.599)	9.07×10^5	2.55×10^6	0.99	1.04	2.73	1.70
2 (0.838)	1.94×10^6	5.83×10^6	0.72	0.52	1.93	0.80

TABLE IV. Quasi-elastic counting rates, and “reduced cross section” as defined by Eq. ???. These rates assume $\Delta t = 12$ hours of running at a beam intensity of $I_{exp} = 30 \mu\text{A}$ on a liquid deuterium target with length $l_{tgt} = 15 \text{ cm}$ and density $d_{tgt} = 0.169 \text{ g.cm}^{-3}$

³⁶¹ The expression of F_2 is:

$$F^2 = \frac{N_{QE}}{\mathcal{L}_{exp} \cdot \Delta t \cdot d\sigma_{Mott}/d\Omega \cdot \Delta\Omega \cdot \eta} \quad (10)$$

³⁶² where Δt the running time, $\Delta\Omega$ is the convoluted BigBite-HCal solid angle, η is the product
³⁶³ of all efficiencies (detection efficiencies $\eta_{det} \times$ selection efficiency η_{sel}) , and \mathcal{L}_{exp} is the
³⁶⁴ experimental luminosity:

$$\mathcal{L}_{exp} = \frac{I_{exp}}{q_e} * L_{tgt} * d_{tgt} \frac{\mathcal{N}_A}{m_D}. \quad (11)$$

³⁶⁵ The calculation of the F_2 term requires the evaluation of the Mott cross section

$$\frac{d\sigma_{Mott}}{d\Omega} = (\hbar c \alpha_{EM})^2 \left(\frac{e}{2E} \right)^2 \left(\frac{\cos\theta_e/2}{\sin^2\theta_e/2} \right)^2 \frac{E'}{E} \quad (12)$$

³⁶⁶ *private note:* $\hbar c$ is in $\text{GeV} \cdot \text{cm}^{-1}$, but I've assumed $e = 1$.

³⁶⁷ The Mott cross section has been calculated with the weighted average of the electron variables
³⁶⁸ (momentum and polar angle).

Point (ϵ)	$\langle \theta_e \rangle$	$\langle k' \rangle$	$\langle Q^2 \rangle$	σ_{Mott}
	(deg)	(GeV)	(GeV 2)	(nb sr $^{-1}$)
1 (0.599)	41.7	2.01	4.47	6.62
2 (0.838)	22.9	4.26	4.40	48.0

TABLE V. Cross-section weighted average of kinematic variables over the BigBite acceptance. The Mott cross section has been evaluated at these values.

³⁶⁹

370

VI. PROPOSED MEASUREMENTS

371 We propose to use the same experimental setup of E12-09-019 experiment. We will add
 372 a kinematic point at $Q^2 = 4.5 \text{ (GeV/c)}^2$, but with a higher ϵ value. This additional point
 373 along with the data point of E12-09-019 experiment will allow us to perform LT separation
 374 and obtain (in one-photon approximation) the G_E^n value. Table 1 displays the kinematic
 375 setting of the proposed experiment.

Point	Q^2 (GeV/c) ²	E (GeV)	E' (GeV)	θ_{BB} degrees	θ_{SBS} degrees	ϵ (%)	$\Delta\sigma$ (%)	ΔTPE (%)
1	4.5	4.4	2.0	41.88	24.67	0.599		
2	4.5	6.6	4.2	23.23	31.2	0.838		

TABLE VI. Kinematic settings of the proposed experiment. The blue row is a kinematic point of E12-09-019 experiment.

376

377

VII. BEAM TIME REQUEST

378 We request 48 hours total time (32 hours of beam-on target) to measure the
 379 two-photon effect (and G_E^n in one-photon approximation) at $Q^2 = 4.5$ (GeV/c) 2 through a
 380 measurement of the cross sections of the reaction D(e,e'N) at a large value of the virtual
 381 photon polarization $\epsilon=0.84$.

382 We plan to take 12 hours of data at a full luminosity of 2.86×10^{38} cm $^{-2}$ s $^{-1}$, which
 383 corresponds to a beam intensity of $I_{exp} = 30 \mu\text{A}$ on a liquid deuterium target with length
 384 $l_{tgt} = 15$ cm and density $d_{tgt} = 0.169 \text{ g.cm}^{-3}$. To have a better handle on our backgrounds,
 385 we also plan to take 12 hours of data at half luminosity (basically by lowering the beam
 386 intensity by a factor 2). In each of these configurations, we also need to take data on a
 387 “dummy” target (*i.e.* on a target cell identical to the one used for production, but empty)
 388 to understand the contamination of our data from the target walls. The projected use of
 389 this time is summarized in Table. VII.

Task	Target	I_{exp}	time requested
Data taking (Prod.)	15 cm LD ₂	30 μA	12 hours
Data taking (Syst.)	15 cm “Dummy”	30 μA	4 hours
Data taking (Prod.)	15 cm LD ₂	15 μA	12 hours
Data taking (Syst.)	15 cm “Dummy”	15 μA	4 hours
Setting change	-	-	16 hours
Total			48 hours

TABLE VII. Summary table for the beam time request.

390

391 This experiment will take place in Hall A, utilizing the BigBite spectrometer to detect elec-
 392 trons scattered off the liquid deuterium target, and HCal calorimeter to detect the recoiling
 393 neutron and proton.

394 Data taking (if approved by PAC48) will take place in summer 2021 during the approved

³⁹⁵ and scheduled run of the GMn, E12-09-019, experiment, which is going to measure the $e - n$
³⁹⁶ elastic scattering cross section at $Q^2 = 4.5$ (GeV/c)² at $\epsilon=0.60$.

³⁹⁷ The set of instrumentation and required beam current for proposed measurement is iden-
³⁹⁸ tical to one in the GMn experiment. The beam energy of 6.6 GeV will be used. One of two
³⁹⁹ data points required for the cross section LT separation is already in the data taking plan of
⁴⁰⁰ GMn.

⁴⁰¹ There are no other measurements of TPE in the $e - n$ elastic scattering and knowledge
⁴⁰² of the TPE is essential for the understanding of the elastic electron scattering from neutron
⁴⁰³ (and proton) and hadron structure. Furthermore, it is a necessary input in the analysis and
⁴⁰⁴ interpretation of a wide range of electron scattering processes.

⁴⁰⁵ The kinematics of our measurements emphasize the same Q^2 range where TPE in $e - p$
⁴⁰⁶ elastic scattering was observed to dominate in Rosenbluth slope. Measuring at this high
⁴⁰⁷ momentum transfers will provide unique input for testing TPE calculations [4].

⁴⁰⁸ We propose to measure the Rosenbluth slope and extract (in one-photon approximation)
⁴⁰⁹ $\delta G_E^n/G_M^n$ to an accuracy of 0.15, which would bring its precision to a level comparable with
⁴¹⁰ that of the double polarization experiments GEN-RP and GEN-He3 at such value of Q^2 .
⁴¹¹ Such precision should be sufficient to detect the TPE contribution to the $e - n$ Rosenbluth
⁴¹² slope on the three sigma level.

-
- 413 [1] R. Hofstadter, *Rev. Mod. Phys.* **28**, 214 (1956).
- 414 [2] M. N. Rosenbluth, *Phys. Rev.* **79**, 615 (1950).
- 415 [3] E. Christy *et al.*, “Two-photon exchange in electron-proton elastic scattering at large four-
416 momentum transfer,” (2020), in preparation for publication in PRL.
- 417 [4] P. G. Blunden, W. Melnitchouk, and J. A. Tjon, *Phys. Rev.* **C72**, 034612 (2005), arXiv:nucl-
418 th/0506039 [nucl-th].
- 419 [5] J. Arrington, P. G. Blunden, and W. Melnitchouk, *Prog. Part. Nucl. Phys.* **66**, 782 (2011),
420 arXiv:1105.0951 [nucl-th].
- 421 [6] A. Afanasev, P. Blunden, D. Hasell, and B. Raue, *Prog. Part. Nucl. Phys.* **95**, 245 (2017),
422 arXiv:1703.03874 [nucl-ex].
- 423 [7] B. Wojtsekhowski, in *Exclusive processes at high momentum transfer. Proceedings, Newport
424 News, USA, May 15-18, 2002* (2002) arXiv:1706.02747 [physics.ins-det].
- 425 [8] G. D. Cates, C. W. de Jager, S. Riordan, and B. Wojtsekhowski, *Phys. Rev. Lett.* **106**, 252003
426 (2011), arXiv:1103.1808 [nucl-ex].
- 427 [9] C. D. Roberts, M. S. Bhagwat, A. Holl, and S. V. Wright, *Eur. Phys. J. ST* **140**, 53 (2007),
428 arXiv:0802.0217 [nucl-th].
- 429 [10] J. Segovia, I. C. Cloet, C. D. Roberts, and S. M. Schmidt, *Few Body Syst.* **55**, 1185 (2014),
430 arXiv:1408.2919 [nucl-th].
- 431 [11] B. Wojtsekhowski (2020) arXiv:2001.02190 [nucl-ex].
- 432 [12] G. A. Miller, *Phys. Rev. Lett.* **99**, 112001 (2007), arXiv:0705.2409 [nucl-th].
- 433 [13] C. E. Carlson and M. Vanderhaeghen, *Phys. Rev. Lett.* **100**, 032004 (2008), arXiv:0710.0835
434 [hep-ph].
- 435 [14] D. Muller, D. Robaschik, B. Geyer, F. M. Dittes, and J. Horejsi, *Fortsch. Phys.* **42**, 101
436 (1994), arXiv:hep-ph/9812448 [hep-ph].
- 437 [15] X.-D. Ji, *Phys. Rev. Lett.* **78**, 610 (1997), arXiv:hep-ph/9603249 [hep-ph].
- 438 [16] A. V. Radyushkin, *Phys. Lett.* **B380**, 417 (1996), arXiv:hep-ph/9604317 [hep-ph].

- ⁴³⁹ [17] M. Diehl and P. Kroll, *Eur. Phys. J.* **C73**, 2397 (2013), arXiv:1302.4604 [hep-ph].
- ⁴⁴⁰ [18] N. Kivel, “private communications,” (2020).
- ⁴⁴¹ [19] E. B. Hughes, T. A. Griffy, M. R. Yearian, and R. Hofstadter, *Phys. Rev.* **139**, B458 (1965).
- ⁴⁴² [20] R. G. Arnold *et al.*, *Phys. Rev. Lett.* **61**, 806 (1988).
- ⁴⁴³ [21] L. Durand, *Phys. Rev.* **115**, 1020 (1959).
- ⁴⁴⁴ [22] E. E. W. Bruins *et al.*, *Phys. Rev. Lett.* **75**, 21 (1995).
- ⁴⁴⁵ [23] G. Kubon *et al.*, *Phys. Lett.* **B524**, 26 (2002), arXiv:nucl-ex/0107016 [nucl-ex].
- ⁴⁴⁶ [24] J. Lachniet *et al.* (CLAS), *Phys. Rev. Lett.* **102**, 192001 (2009), arXiv:0811.1716 [nucl-ex].
- ⁴⁴⁷ [25] V. Punjabi, C. F. Perdrisat, M. K. Jones, E. J. Brash, and C. E. Carlson, *Eur. Phys. J.* **A51**, 79 (2015), arXiv:1503.01452 [nucl-ex].
- ⁴⁴⁸